TEMPERATURE EFFECTS ON THE FATIGUE CHARACTERISATION OF A CARBON-EPOXY COMPOSITE MATERIAL

G. Charalambous*, G. Allegri

Advanced Composite Centre for Innovation and Science (ACCIS),
University of Bristol, Bristol, BS8 1TR, UK
**Georgia.Charalambous@bristol.ac.uk*

Keywords: Mixed-Mode Fracture, Fatigue, Delamination, Temperature

Abstract
An experimental investigation of the effects of temperature on the fracture toughness and mixed-mode fatigue delamination growth in an aerospace grade fibre reinforced polymer, namely IM7/8552, is presented. All the characterization tests have been performed using asymmetric cut-ply specimens subjected to four-point bending both at room and elevated temperatures. It is demonstrated that the mixed-mode fracture toughness increases with the temperature, while the delamination propagation rates decreases at higher severities and increases at lower severities. A new semi-empirical equation describing the effects of temperature on the delamination growth rates is proposed.

1 Introduction

Fibre reinforced composites are increasingly employed in primary structural elements in several fields of engineering, including aerospace, automotive, naval and civil. Fibre reinforced composites have excellent in-plane specific mechanical properties, but they are prone to delamination due to their limited out-of-plane strength. Moreover composite laminates usually comprise features that act as interlaminar stress raisers e.g. free-edges and ply drop-offs, leading to the onset and growth of delaminations. This implies that the onset of interlaminar cracks is somehow unavoidable and that a damage tolerance design philosophy should be adopted. Thus robust engineering models for the prediction of fatigue delamination growth are needed. These must include also the effect of the operative environment, temperature in the first place.

Fatigue delamination growth rates (FDGR) are usually described via power laws that comprise the energy release rate (ERR) attained at the delamination tip as independent variable [1]. However it has been observed that temperature has a major influence on the coefficients that appear in the aforementioned power laws [2-8]. The magnitude and nature of such influence strongly depends on the specific nature of the polymer constituting the matrix and the glass transition temperature T_g of the latter. If the testing temperature is below T_g, one usually observes a progressive increase of the fracture toughness with raising temperatures, as well as a reduction of the FDGR at constant ERR. This behaviour is usually explained by observing that for temperatures tending to the T_g polymers exhibit enhanced ductility, while cryogenic conditions lead to embrittlement. Clearly there exists a wide range of possible

intermediate behaviours between these two extremes. Temperature effects also seem to depend on the mode-mixity, albeit there is no consensus in the literature [9-12] about which fracture mode is the most affected by temperature and why. Actually many additional features may contribute to the effect of temperature on toughness and FDGR in fibre reinforced plastics, e.g. presence toughening agents in the matrix, nature of the fibres and residual stresses within the laminate, just to mention just a few.

In the literature, several different specimen configurations have been proposed for the characterization of fracture toughness and FDGR in uni-directional composite laminates. Some of these have been incorporated into testing standards [13]. Double cantilever bending (DCB) and end-notch flexure (ENF) specimens are employed respectively for mode I and mode II toughness measurements. Either Mixed-mode bending (MMB) or end-loaded split (ELS) specimens [14] can be employed for characterizing mixed-mode fracture. It is worth observing that, strictly speaking, the standardization of the testing methodologies mentioned above has been carried out only for the static cases, i.e. toughness measurements. For FDGR there are no available standards, albeit in most of the relevant literature the standard "static" specimen configurations are employed in fatigue. However this poses some issues, particularly for mixed-mode cases: MMB and ELS loading jigs are quite complex and prone to fatigue themselves. The delamination length measurement is carried out via a compliance calibration and/or "in-situ" optical measurement of the crack front position. The overall process is time consuming and error prone.

Lander et al. [15] proposed to employ asymmetric cut-ply (ACP) specimens subjected to four point bending for the characterization of the mixed-mode fracture toughness of uni-directional composite laminates. The ACP specimen configuration is essentially an extension of the single-edge notched bending (SENB) layout to laminated composites [16]. The main advantage offered the ACP layout is that no compliance calibration is required to obtain the fracture toughness and this simplifies the testing. Moreover four-point bending jigs are relatively simple and robust.

In this paper ACP specimens are employed to characterize the effect of temperature on the toughness and FDGR in the carbon fibre-reinforced epoxy IM7/882. It is demonstrated that no compliance calibration is required for both the static and the fatigue tests. Also a new semi-empirical equation that describes the effect of temperature on the FDGR is introduced.

2 Asymmetric Cut Ply Specimens (ACP)

2.1 Energy release rate and mode-mixity

The ACP configuration is sketched in fig. 1. The specimen comprises a mid-section cut, which extends from the surface to a prescribed depth t_1. Let χ denote the ratio of the cut depth to the overall specimen thickness $t = t_1 + t_2$. For plies having constant thickness, as in the case considered here, χ simply represents the ratio of the number of cut plies to the total number of plies. An insert having total length $2a$ is placed symmetrically beneath the cut, thus simulating the presence of a $2a$ long delamination, which is allowed to propagate along the overall specimen gauge length $2L$.

Following the procedure outlined in ref. [15], the mode I G_I and mode II G_{II} ERR for the ACP specimen are given by:

$$G_I = \frac{6M^2}{Et^3}\frac{\psi}{\chi^3+(1-\chi)^3} \tag{1}$$

$$G_{II} = \frac{6M^2}{Et^3}\left[\frac{1}{\chi^3+(1-\chi)^3}-1\right] \tag{2}$$

Where E is the material longitudinal Young's modulus, M is the applied bending moment and

$$\psi = \frac{\chi^3}{(1-\chi)^3} \tag{3}$$

The total ERR is given by

$$G = \frac{6M^2}{Et^3}\left[\frac{1}{(1-\chi)^3}-1\right] \tag{4}$$

Therefore for the mode-mixity one has

$$\phi = \frac{G_{II}}{G} = \frac{3(1-\chi)^4}{(1-3\chi+3\chi^2)(3-3\chi+\chi^2)} \tag{5}$$

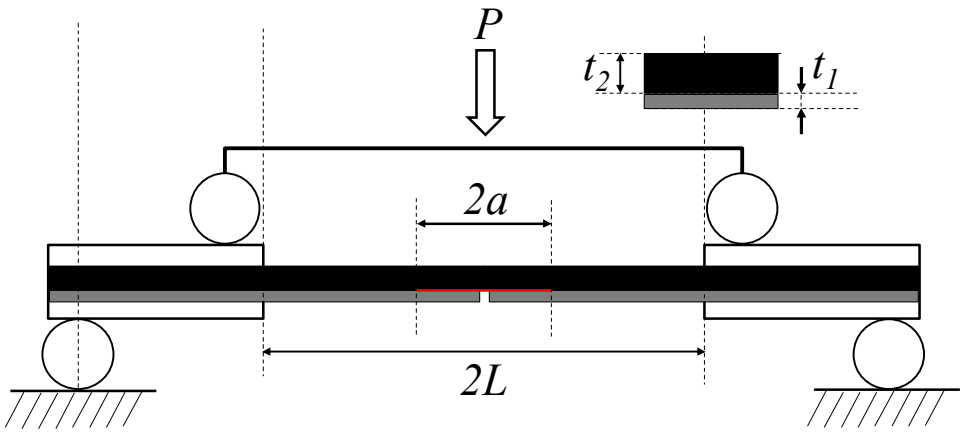

Figure 1: Asymmetric Cut-Ply Bi-Material Specimen in 4 point bending.

From eqs. (1)-(5) one can immediately observe that, given a constant applied bending moment M, the ERR in ACP specimens is independent from the crack length and so is the mode-mixity. Actually the latter depends only on the thickness ratio χ so it is possible to adjust the values of ϕ simply by changing the number of cut plies with respect to the total number of plies in the specimen. If χ is small, then $\phi \to 1$, i.e. a pure mode II regime tends to be attained. On the other hand for $\chi \to 1$ one finds $\phi \to 0$, so the delamination tends to grow in mode I dominated conditions. Clearly there are practical limitations on the range of χ, because cutting a large number of plies would make the specimen extremely compliant. Similarly in order to approximate mode II it is necessary to make the specimen relatively thick, which invalidates the assumption of zero through thickness shear strains on which the ERR and mode-mixity expressions given in eqs. (1)-(5) are based [15].

2.2 Large rotation correction

Since the ACP specimen is subjected to four-point bending, large rotations can occur at the end tabs. This implies that the relation between the bending moment M acting at the delamination tip and the applied force needs to account for such large rotations.

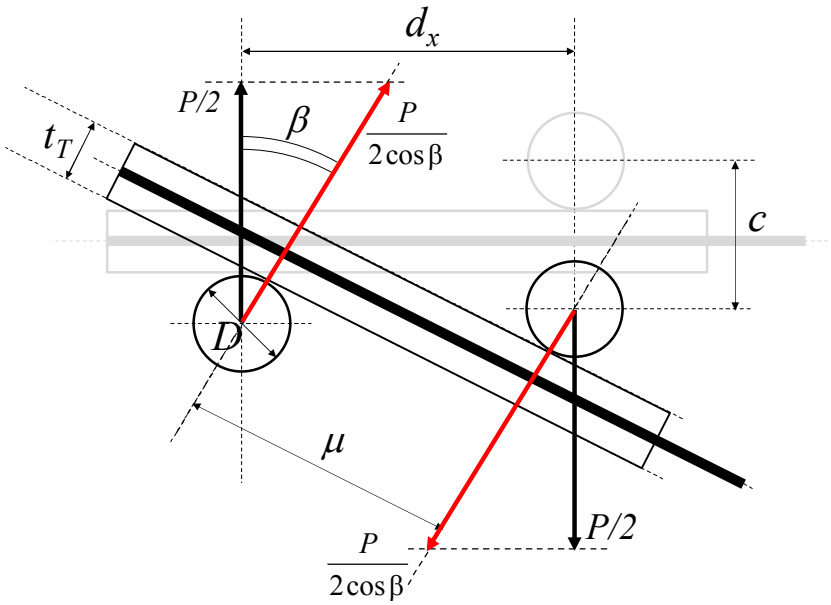

Figure 2: Specimen rotations and associated forces at the rollers.

As sketched in fig. 2, due to the rotation angle β the actual force applied by the roller onto the specimen is given by:

$$F = \frac{P}{2\cos\beta} \tag{6}$$

On the other hand the arm between the applied force on the loading roller and the reaction force on the static roller is given by:

$$\mu = \frac{d_x}{\cos\beta} - \left(D + t_T\right)\tan\beta \tag{7}$$

Where D is the roller diameter and t_T is the thickness of the tabbed region. Therefore the actual bending moment per unit width applied during the test is a function of the specimen rotation between the rollers and it is given by:

$$M = \frac{F\mu}{W} = \frac{P}{2W\cos^2\beta}\left[d_x - \left(D + t_T\right)\sin\beta\right] \tag{8}$$

Where W is the specimen width. Assuming the bending and shear deformations in the tabbed area of the specimen are negligible; it is possible to estimate the specimen rotation by means of the cross-head displacement c only, using the following equation:

$$\tan\beta = \frac{c - \left(D + t_T\right)\left(1 - \cos\beta\right)}{d_x - \left(D + t_T\right)\sin\beta} \tag{9}$$

Which has to be solved iteratively. Substituting the solution of eq. (9) into eq. (8) for a given load cell force P and cross-head displacement c yields the corrected applied bending moment M.

2.3 Estimation of delamination length and growth rates

It is here assumed that fatigue delamination growth tests are carried out in a displacement controlled regime. In this case it is possible to derive the delamination growth rates directly from the cross-head displacement and load-cell force readings, provided that the loading jigs are sufficiently stiff for and the compliance of the machine is negligible. Let a sinusoidal load be applied to the specimen. The deformed shape of the specimen under loading is described by the following equations

$$\frac{d\hat{\theta}}{ds} = \begin{cases} \dfrac{\hat{M}W}{EI\left(1-\chi^3\right)} & 0 \le s \le a \\ \dfrac{\hat{M}W}{EI} & a < s \le L \end{cases} \tag{10}$$

Where, as shown in fig. 3, $\hat{\theta}(s)$ is the rotation of the beam section, s is a curvilinear abscissa defined along the deformed beam axis, a is the delamination length, $\hat{M}$ is the peak applied bending moment and $I = 1/12Wt^3$ is the cross-sectional second moment of area. Let θ^* be the specimen rotation at the delamination tip position $s = a$ and corresponding to the peak bending moment. Note that the rotation at the mid-plane, i.e. for $s = 0$ is zero, while the rotation at the loading roller, i.e. $s = L$, is $\hat{\beta}$ given by eq. (24) solved for the peak cross-head displacement $\hat{c}$ during the fatigue cycle. In principle any point during the fatigue cycle could be considered for the crack length measurement, but at the peak bending moment the force applied by the machine is maximum and so the load-cell measurement less prone to linearity errors. Also it should be observed that there will always be a delay between the time at which the peak force is applied and that for maximum displacement. This is due to the inherent

damping in the specimen, so care must be taken in recording the correct peak force and displacement values. Integrating eq. (10) one gets:

$$\theta^* = \frac{\hat{M}W}{EI(1-\chi)^3}a \qquad (11)$$
$$\hat{\beta} - \theta^* = \frac{\hat{M}W}{EI}(L-a)$$

Combining eqs. (11) and solving with respect to the crack length yields:

$$a = k(\chi)\left[\frac{\hat{\beta}EI}{\hat{M}W} - L\right] \qquad k(\chi) = \frac{(1-\chi)^3}{1-(1-\chi)^3} \qquad (12)$$

Since the test is run in a displacement control regime (i.e. for a constant peak cross head displacement $\hat{c}$), $\hat{\beta}$ is constant in eqs. (11)-(12) by virtue of eq. (9).
Thus for the crack growth rate measured in a displacement controlled test one has:

$$\frac{da}{dN} = -k(\chi)\frac{\hat{\beta}EI}{W\hat{M}^2}\frac{d\hat{M}}{dN} \qquad (13)$$

Note that in in eq. (14) the peak bending moment decreases with the number of load cycles, since the crack length increases and so does the specimen compliance. Therefore in eq. (13) one has $d\hat{M}/dN < 0$ and the resulting delamination growth rate is positive. Substituting eq. (8) evaluated at the peak load into eq. (13) yields the delamination growth rate as a function of the applied load

$$\frac{da}{dN} = -\frac{k(\alpha)}{2W\cos^2\hat{\beta}}\left[d_x - (D+t_T)\sin\beta\right]\frac{\hat{\beta}E^*I^*}{W\hat{M}^2}\frac{d\hat{P}}{dN} \qquad (14)$$

Where $\hat{\beta}$ is obtained from eq. (9) evaluated at the peak cross-head displacement.

Again in eq. (14) one has $d\hat{P}/dN < 0$, since when the delamination propagates the specimen compliance increases. This proves that using ACP specimens it is possible to measure the FDGR during a fatigue test by means of the load-cell readings and the cross-head displacements alone.

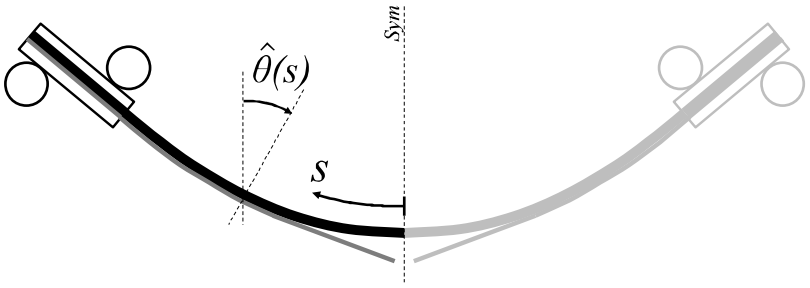

Figure. 3: Specimen deformed configuration.

3 Experimental Testing

3.1 Specimen manufacturing

Uni-directional ACP specimen were manufactured using Hexcel® IM7/8552 carbon fibre-reinforced epoxy. The specimens comprised ten plies, out of which five were cut, giving $\chi = 1/2$. The nominal cured ply thickness for IM7/8552 is 0.127 mm, giving a total specimen nominal thickness of 1.27 mm. The actual thickness measured on the coupons was within 2% the nominal value. Uni-directional IM7/8552 has a Young's modulus E = 161 GPa.

The total specimen length was 190 mm, with a gauge section of $2L$ = 90 mm and a width W = 15 mm. The tabbed areas extended for 50 mm at both the ends of the gauge section. The tabs were manufactured using E-Glass/Epoxy 950 pre-preg arranged in a cross-ply stacking. The manufacturing process consisted of the lay-up and vacuum consolidation of two initially individual ply-stacks made of 5 plies each. One of the two stacks had been cut in half. A 20mm long, 12.7μm thick and 15mm wide PTFE film was embedded at the centre of the first ply-stack and subsequently covered with the second ply-stack. Thus the film inserts simulates the presence of an initial delamination $2a$ = 20mm long. The two halves of the cut stack were tightly pushed together along the cut line, so no central gap is formed. The full laminate was de-bulked in vacuum at room temperature for 20 minutes and then cured in the autoclave. The tabs were then bonded to the specimens using the Redux 810 bi-component epoxy adhesive. The total thickness of the specimen in the tabbed areas was 6.4 mm.

After curing it was observed that a vertical resin bridge had formed at the cut location, joining the two laminate halves and preventing the delamination from opening. The resin join was fractured applying a low level of tension to the specimen, taking care that, in the meanwhile, no delamination propagation occurred. The specimens were kept in desiccators' cabinet prior to testing.

In the literature it is reported that artificial delaminations created by the insertion of thin films may affect the measured value of the fracture toughness. O'Brien [17] considered ENF specimens with Teflon inserts having the same thickness of those considered here. He carried out static fracture tests both by growing the delamination directly from the insert and pre-cracking the coupons by applying fatigue cycles before the static tests. He reported that the mode II fracture toughness of IM7/8552 was 50% higher for non-pre-cracked (NPC) ENF coupons compared with pre-cracked (PC) ENF specimens. Thus growing delamination directly from the film insert may lead to an overestimation of the actual material fracture toughness. Such effect is likely due to the fact that the delamination tip for NPC specimens is blunted by the presence of the insert, thus increasing the measured fracture toughness of the material with respect to PC coupons, for which the crack front is sharp.

In order to take into account the possible enhancement of the mixed-mode fracture toughness due to the presence of the thin films, NPC and PC specimens are also considered here for the room temperature tests. The pre-cracking was carried out by symmetrically clamping the specimen with metal blocks at a set distance of 20mm from the central cut. A force was applied at the cut location on the face opposite to the cut itself until the delamination had symmetrically grown to the inner edges of the clamping blocks. The procedure was repeated until both sides of the specimen propagated the same amount. C-scans were performed after

the pre-cracking in order to check that the position of the delamination front was uniform across the specimen width. A sample of the C-scans is presented in fig. 4.

3.2 Experimental Procedure

The four-point bending tests were carried out using a jig with roller distance $d_x = 25$mm. The loading jig is shown in fig. 5. It comprises a long push rod in order to be used within an environmental chamber for testing at variable temperature. The correct positioning of the sample within the test rig is of crucial importance for the test accuracy. Therefore an alignment tool was manufactured to ensure that the cut position was exactly in between the loading rollers. The specimen configuration considered here consists in five cut plies out of a total of ten. Therefore eq. (5) yields a mode-mixity $\phi = 0.43$. The static fracture toughness was determined for NPC and PC coupons at room temperature, i.e. 20°C, 50°C and 80°C. A minimum of three specimens were tested in each case.

The fatigue tests were run in displacement control, starting from a displacement corresponding to 80% of the static strength, with a constant stress ratio $R = 0.1$. Again three temperatures were considered, namely 20°C, 50°C and 80°C. Each test was performed using a sinusoidal displacement input with a frequency of 5 Hz and for a total 10^6 cycles.

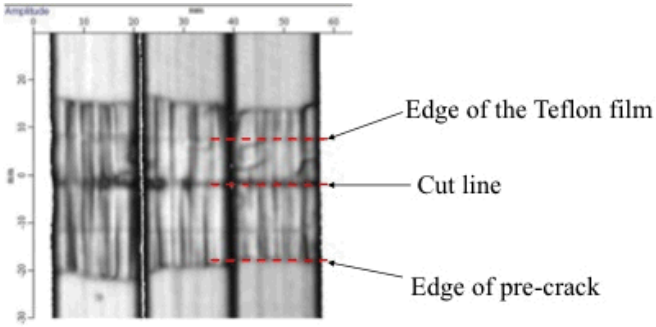

Figure. 4: C-scans of pre-cracked specimens.

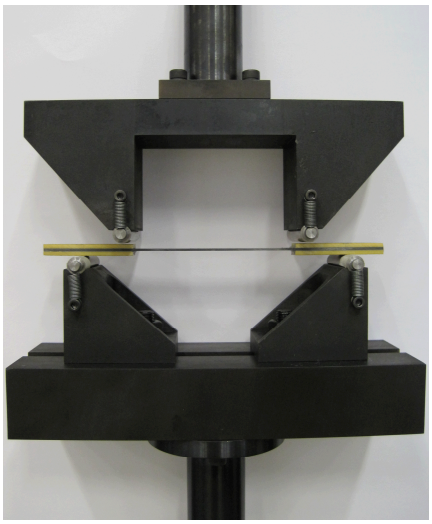

Figure. 5: 4-point loading jig employed for the static and fatigue tests

4. Results and discussion

4.1 Static Tests

The static tests for the characterization of the fracture toughness were carried out in displacement control mode. The ensemble bending moment versus cross-head displacement curves recorded during the tests are presented in fig. 6-8 for the NPC cases, while a summary of the fracture toughness values obtained is given in tab. 1. The bending moment was calculated from the individual load-displacement curves using the large rotation correction presented in sec. 2.2.

From the NPC tests carried out at 20°C and presented in fig. 6, one can observe that the applied bending moment increases almost linearly until an average peak load value of 80 N is reached at an average displacement of 5.8 mm. This marks the onset of static delamination growth. Note that the bending moment is here given per unit width. Further increasing the displacement beyond the delamination onset threshold leads to a bending moment plateau which corresponds to an observed stable symmetric delamination growth with respect to the central cut. Thus the bending moment is independent from the crack length, as predicted by the analytical solution given in eq. (4). Inserting the experimental value of the bending moment for delamination propagation into eq. (4) allows calculating the material mixed-mode fracture toughness. The load-displacement curves for the tests carried out on PC specimens at room temperature followed exactly the same trend observed for the NPC specimens and the associated bending moment for delamination growth show no statistically significant difference from that obtained for the NPC coupons. As a consequence, the values of mixed-mode fracture toughness reported in tab. 1 for NPC and PC specimens are statistically identical. Since the pre-cracking has no effect on the measured toughness values at 20°C, only NPC coupons were considered for the static fracture characterization at 50°C and 80°C.

Increasing the temperature has a significant impact on the way delamination propagate under static loading. At 50°C the delamination grew in a "stick-slip" regime, with discrete jumps in length followed by reloading phases. Increasing the testing temperature to 80°C further exacerbated this behaviour, since no symmetric delamination growth is observed beyond the cross-head displacement corresponding to the peak bending moment.

	20°C		**50°C**	**80°C**
	NPC (8)[(a)]	**PC (3)**[(a)]	**NPC (8)**[(a)]	**NPC (5)**[(a)]
G_c (kJ/m^2)	0.399 (0.034)[(b)]	0.3919 (0.053)[(b)]	0.854 (0.136)[(b)]	1.130 (0.289)[(b)]

[(a)] Number of specimens tested

[(b)] Standard deviation of the fracture toughness

Table 1: Experimental mixed-mode fracture toughness for IM7/8552; $\phi = 0.43$.

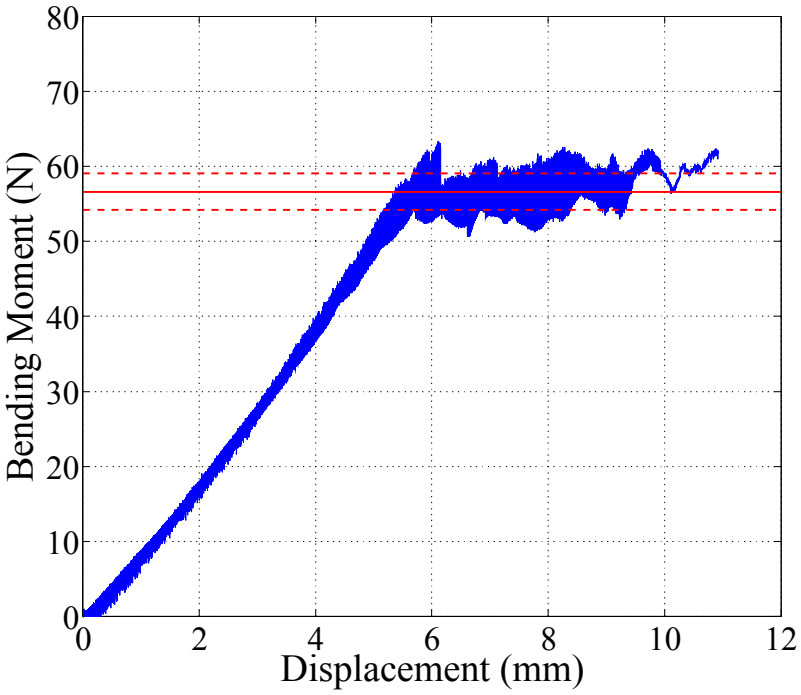

Figure. 6: Bending moment vs. displacement curves for NPC specimens at 20°C;
average bending moment for delamination growth in red continuous line;
Red dashed lines give the standard deviation of the bending moment for delamination growth.

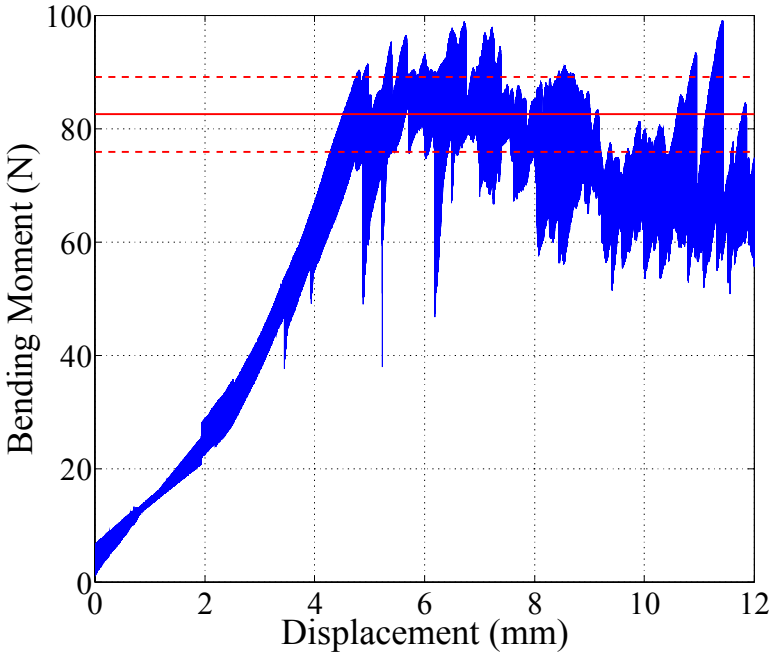

Figure. 7: Bending moment vs. displacement curves for NPC specimens at 50°C;
average bending moment for delamination growth in red continuous line;
Red dashed lines give the standard deviation of the bending moment for delamination growth.

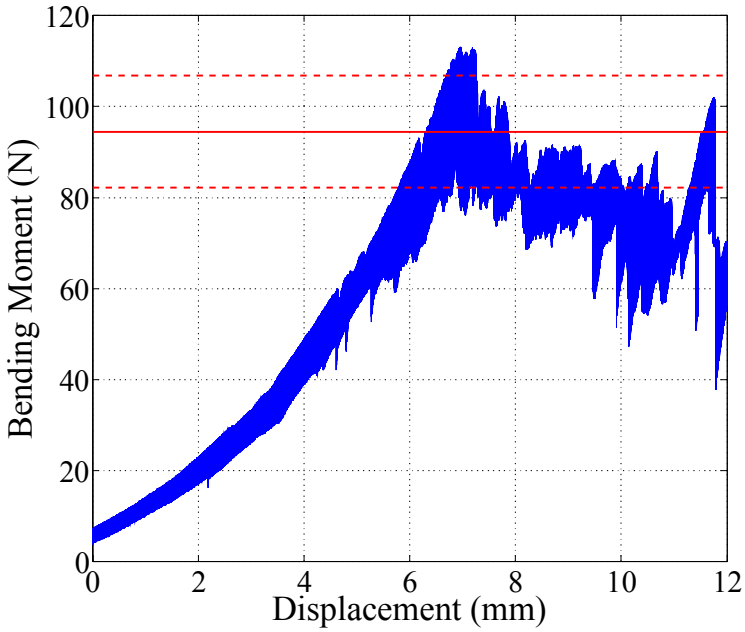

Figure. 8: Bending moment vs. displacement curves for NPC specimens at 80°C;
average bending moment for delamination growth in red continuous line;
Red dashed lines give the standard deviation of the bending moment for delamination growth.

The different nature of static delamination growth with respect to temperature can be easily appreciated considering the bending moment versus displacement curves presented in fig. 7 and 8. It is worth observing that the slope of the load-displacement curves in the linear region before delamination growth is the same at the three temperatures considered, so the temperature increase had no significant effect on the material Young's modulus *E*. This has to be expected, since the flexural stiffness for uni-directional specimens is fibre dominated and the stiffness of carbon fibres is not significantly affected by temperature variations in the 60°C range considered here.

From fig. 7, one can observe that the extent of the symmetric propagation plateau region at 50°C is considerably smaller than at 20°C. The region where the bending moment appears to drop is that of asymmetric delamination growth, where the formulas given in eqs. (4) and (8) are not applicable any more. For the 80°C tests presented in fig. 8, as mentioned above, no symmetric delamination growth was observed. Moreover dynamic effects due to the "stick-slip" behaviour also made the load cell signal considerably noisier than in the 20°C case. Since for the calculation of the ERR according to eqs. (4) and (8) symmetric delamination growth is required, for the 50°C tests the ERR estimation was carried out considering only the portions of the load-displacement curves where equal interlaminar crack lengths with respect to the central cut were actually observed. On the other hand, for the 80°C tests the ERR was estimated considering the average peak value of the applied bending moment, since delaminations grew only asymmetrically with respect to the central cut.

A summary of the toughness values calculated from the tests is presented in tab. 1. Raising the testing temperature to 50°C doubled the material mixed-mode fracture toughness. At 80°C the fracture toughness is almost three times that measured at 20°C.

4.2 Fatigue Tests

During the fatigue tests, the cross-head displacements and load cell force were recorded every five cycles. Eq. (13), or equivalently eq. (14), allows computing the delamination growth rate directly from the aforementioned data. The delamination growth observed during the tests was generally stable, with the noteworthy exception of the first few hundred cycles for the 50°C and 80°C. In these cases the crack initially propagated very fast, i.e. at about 10^{-2} mm/cycle, exhibiting asymmetric length increments with respect to the central cut. This "stick-slip" propagation mechanism at relatively large applied loading was analogous to that observed during the static tests, albeit less severe. When the delaminations reached a length of approximately 15 mm with respect to central cut, the further growth occurred symmetrically with respect to the central cut and the "stick-slip" behaviour disappeared.

It is worth observing that both eq. (13) and (14) comprises a derivative term of the applied load, either the bending moment or the load-cell force. The load-cell measurement of the applied force is affected by noise and computing its numerical derivative directly from the test data introduces further errors. The same is true for the bending moment, which in displacement controlled tests is just proportional to the applied force as pointed out by eq. (8). In order to mitigate the influence of the load-cell noise on the FDGR estimation, the bending moment corresponding to each load-cell recording was computed using eq. (8) and then interpolated employing the following exponential function

$$M = \beta_1 + \left(1 - \beta_1\right) e^{-\beta_2 N^{\beta_3}} \tag{15}$$

Where N is the number of applied load cycles and $\beta_i \quad i = 1, 2, 3$ are real valued coefficients.

The latter were estimated via a nonlinear regression of the experimental data on the model function given in eq. (15). This was carried out employing the "NLINFIT" routine available in MATLAB®. Fig. 9 shows an example of the level of accuracy achieved by employing the interpolation scheme described above. Clearly the nonlinear regression has to be repeated on the data recorded for each of the tests. Once the interpolation parameters $\beta_i \quad i = 1, 2, 3$ had been identified via the nonlinear regression, the delamination growth rates were computed using eq. (13) by considering the derivative of eq. (15) in analytical form.

A summary of the results of the fatigue tests is presented in fig. 10. Here the FDGR are plotted against the peak ERR $\hat{G}$ applied during the test. Due to the unstable nature of the crack propagation at the beginning of the fatigue tests for the 50°C and 80°C cases, the FDGR values considered in the summary chart in fig. 10 have been limited to 10^{-3} mm/cycle. Above this value the load-cell signals are extremely noisy and it is not possible to extract statistically meaningful information from the raw test data.

From fig. 10 one can observe that at higher severities, i.e. for relatively large $\hat{G}$ values, the fatigue delamination growth is delayed when the temperature is increased. Moreover the slope of the FDGR decreases significantly with temperature. However the FDGR curves cross at a peak ERR of about 0.22 kJ/m^2. Therefore at the lower severities, i.e. in a near threshold regime, the FDGR at 50°C and 80°C are larger than those characterizing the delamination

propagation at 20°C. This effect is extremely important from an engineering point of view, since the near threshold regime is that usually considered for the damage tolerance design of composite structural elements. Fig. 10 proves that an increase in static fracture toughness does not necessarily correspond to a better performance in fatigue in the case where a near threshold regime is considered.

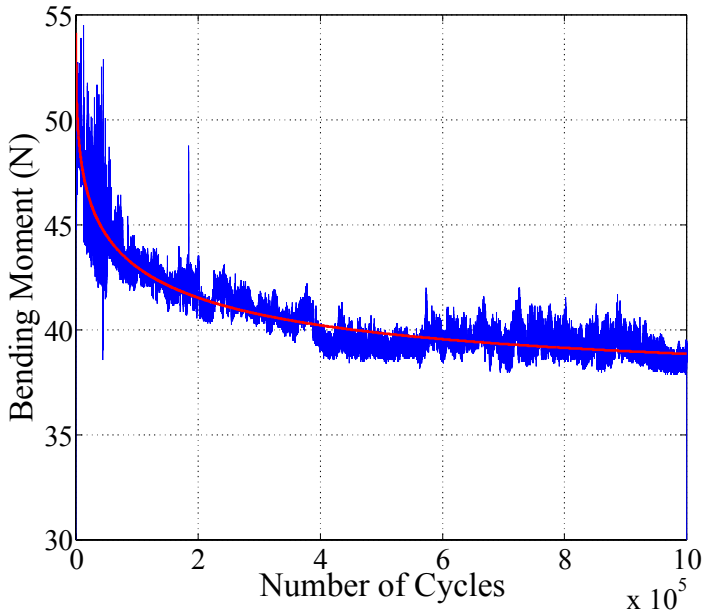

Figure 9: Data reduction via the interpolation function in eq. (15); NPC specimen at 20°C; Experimental bending moment in blue line and interpolation in red line

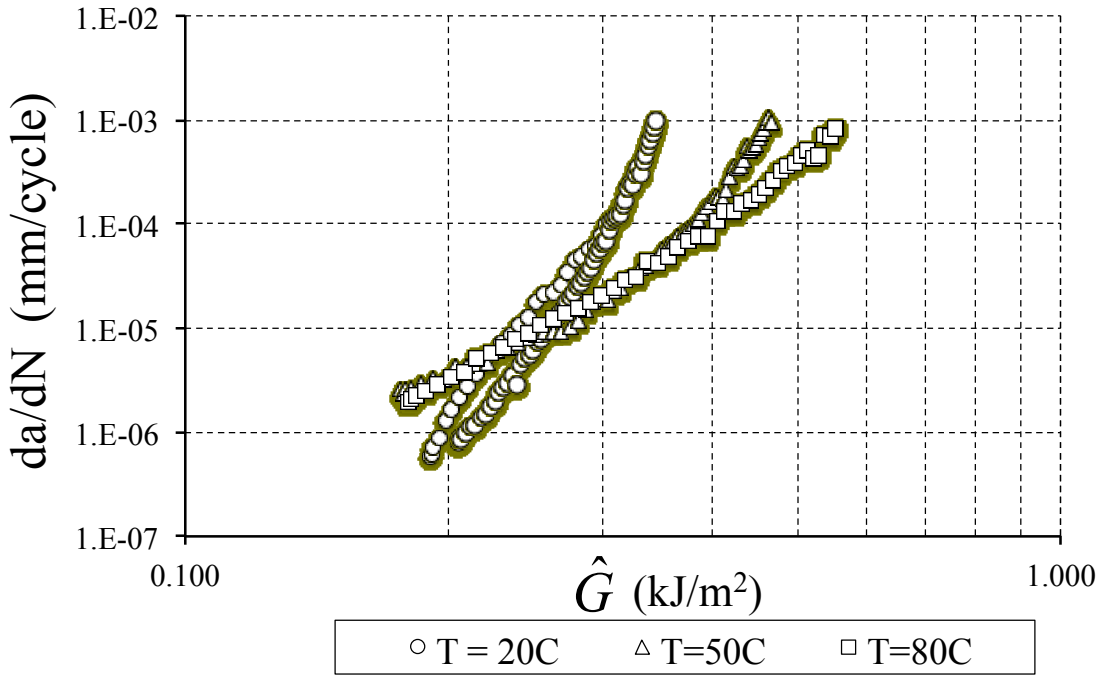

Figure 10: Delamination growth rates as functions of the peak ERR.

4.3 Semi-empirical fatigue delamination growth law

An alternative presentation of the experimental data obtained during the fatigue tests is shown in fig. 11. Here the peak energy ERR $\hat{G}$ is normalized with respect to the static fracture toughness values for each temperature, as given in tab. 1. The FDGR curves with respect to the normalized ERR do not intersect any more and they are spaced apart on the chart plane. In order to represent the data in fig. 11, the following semi-empirical equation is proposed

$$\frac{da}{dN} = C\left(\frac{\hat{G}}{G_c}\right)^{b\left(\frac{T_0}{T}\right)^{\gamma}} \tag{16}$$

Where C, b and γ are material dependent fatigue parameters, T is the testing temperature and T_0 an arbitrary reference temperature.

When $T = T_0$, the semi-empirical equation given in eq. (16) reduces to a standard Paris crack propagation power law [1]. Therefore, for the fatigue data set considered here, setting $T_0 =$ 20°C allows identifying the material coefficients C and b directly from the room temperature tests. Once C and b are known, γ is estimated from the experimental FDGR at $T \neq T_0$ via a nonlinear regression based on the modified power law in eq. (16). In principle, a single FDGR curve at $T \neq T_0$ is sufficient for estimating γ and so the FDGR trends for arbitrary temperatures, provided that the associated fracture toughness is known. However the emphasis here is not on demonstrating the predictive capabilities of eq. (16), but on proving that it represents a suitable data reduction tool for describing the temperature effect on FDGR.

Considering the mathematical form of eq. (16), one can observe that in double logarithmic axes it describes a locus with all lines intersecting at the point of abscissa $\hat{G}/G_c = 1$ and ordinate C. These lines described the stable fatigue propagation regime of delaminations at arbitrary temperatures. The slope of the lines is inversely proportional to T^{γ}, so it decreases when the temperature increases. This produces a clockwise rotation of the FDGR lines in double logarithmic axis with increasing temperature; the rotation takes place with respect to a pivot point that represents static fracture according to the Griffith criterion, i.e. $\hat{G}/G_c = 1$. When $\hat{G}/G_c = 1$ the FDGR is nominally infinite, but clearly eq. (16) can represent only stable delamination growth.

From a qualitative point of view, one can observe that the FDGR curves in fig. 11 indeed rotate clockwise when the temperature is increased. However the existence of a common projected intersection at $\hat{G}/G_c = 1$ is debatable. Actually the data for the 50°C do not lie on a standard Paris law trend, but this is due to the fact that only one specimen has been tested and the data set is still too sparse. Therefore further experimental tests are required to validate eq. (16).

Performing a non-linear regression of the experimental data by means of the model function given in eq. (16) yields the following material temperature-dependent parameters

$$C = 4.4 \times 10^{-3}\,\text{mm/cycle}; \qquad b = 12.90; \qquad \gamma = 0.943 \tag{17}$$

The interpolated trends given by eq. (16) with the coefficients from eq. (17) are shown in fig. 11 as continuous black lines. The quality of the fit is satisfactory, being the overall coefficient of determination at 90%.

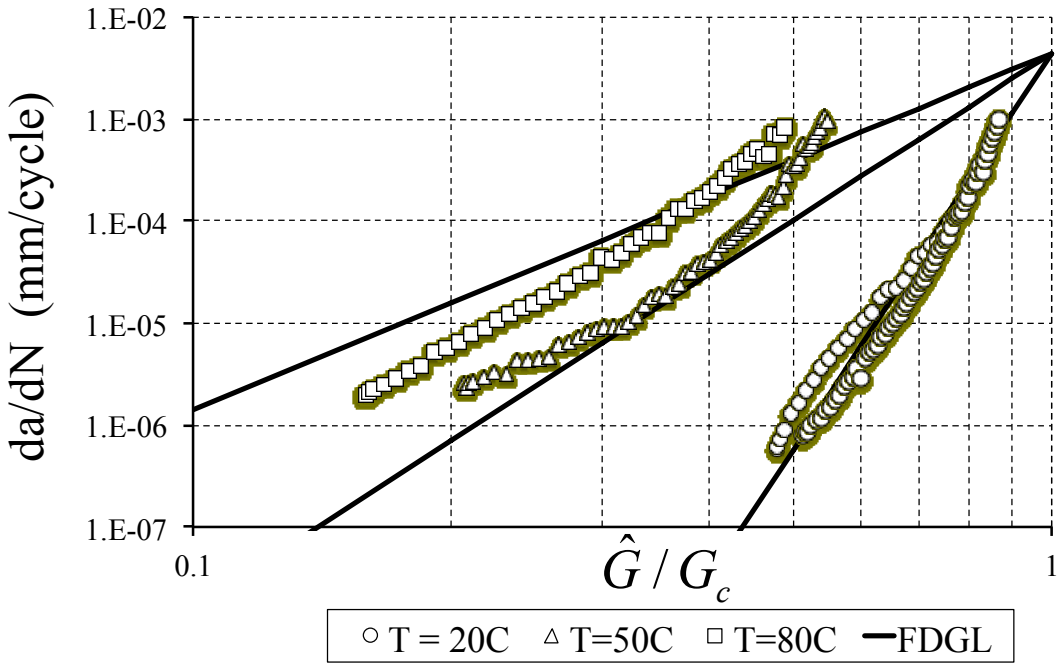

Figure 11: Delamination growth rates as functions of the peak normalized ERR;
FDGL are the predicted trends from the semi-empirical fatigue delamination growth law in eq. (16).

6 Conclusions

The mixed-mode fracture toughness of IM7/8552 has been characterized using ACP specimens. Three testing temperatures have been considered, namely 20°C, 50°C and 80°C. A strong increase of the fracture toughness with temperature has been observed for the aforementioned material. The fracture toughness at 50°C is double that measured at 20°C; further increasing the temperature to 80°C raises the fracture toughness threefold with respect to the 20°C datum. The increase in fracture toughness is accompanied by a transition from a progressive stable delamination growth to a "stick-slip" regime, where the delamination advances in discrete unstable length increments. No differences in fracture toughness were observed when growing the delamination directly from the insert film with respect to pre-cracking the specimens.

ACP specimens have also been employed for characterizing the mixed-mode fatigue delamination growth in IM7/8552 as a function of the testing temperature. The experimental results point out that, at relatively high severities, increasing the temperature delays the fatigue delamination growth. The opposite effect is observed at low severities, i.e. in a near threshold regime, where increasing the temperature actually speeds up the fatigue delamination propagation.

A new semi-empirical power law with a temperature dependent exponent has been introduced to describe the effect of temperature on fatigue delamination growth. The semi-empirical

model provides a satisfactory fit of the experimental data, although further tests are still required to fully validate it.

Acknowledgements

The authors would like to acknowledge the support of Rolls Royce Plc through the Composites University Technology Centre of the University of Bristol.

References

[1] O'Brien, T.K., Characterization of delamination onset and growth in a composite laminate. In: Damage in Composite Materials, ASTM STP 7, pp. 141-167, 1981.

[2] Sjögren, A., and Asp, L.E., Effects of temperature on delamination growth in a carbon/epoxy composite under fatigue loading, International Journal of Fatigue, 24, pp. 179-184, 2002.

[3] Dennis, A., Burianek, S., and Spearing, S.M., Delamination growth from face sheet seams in cross-ply titanium/graphite hybrid laminates, Composites Science and Technology, 61, pp. 261-269, 2001.

[4]M. Miura, Y. Shindo, F. Narita, S. Watanabe, M. Suzuki. Mode III fatigue delamination growth of glass fiber reinforced polymer woven laminates at cryogenic temperatures, Cryogenics 2009;49:407-412

[5] Hojo, M., Matsuda, S., Fiedler, B., Kawada, T., Moriya, K., Ochiai, S. and Aoyama, H., Mode I and II delamination fatigue crack growth behavior of alumina fiber/epoxy laminates in liquid nitrogen, Int. j. Fatigue, 24, pp. 109-118, 2002

[6] Shindo, Y., Inamoto, A., Narita, F. and Horiguchi, K., Mode I fatigue delamination growth in GFRP woven laminates at low temperatures, Eng. Fracture Mech, 73 pp. 2080–2090, 2006.

[7] Shindo, Y., Takeda, T., Narita, F., Saito, N., Watanabe, S., and Sanada, K., Delamination growth mechanisms in woven glass fiber reinforced polymer composites under Mode II fatigue loading at cryogenic temperatures, Comp. Sci. Tech., 69, pp. 1904–1911, 2009.

[8] Shindo, Y., Shinohe, D., Kumagai, S., and Horiguchi, K., Analysis and Testing of Mixed-Mode Interlaminar Fracture Behaviour of Glass-Cloth/Epoxy Laminates at Cryogenic Temperatures, J. Eng. Mater. Technol., 127(4), 468-475, 2005.

[9] Cowley, K.D., and Beaumont, P.W.R., The interlaminar and intralaminar fracture toughness of carbon fibre/polymer composites: The effect of temperature, Comp. Sci. Tech., 57, pp. 1433-1444, 1997.

[10] Wagner, H.D., Tuler, F.R., and Marom, G., Time and temperature dependence of fracture in a unidirectional glass-reinforced epoxy, Polymer, 20(5), pp. 653-658, 1979.

[11] Asp, L.E., The effects of moisture and temperature on the interlaminar delamination toughness of a carbon/epoxy composite, Comp. Sci. Tech., 58, pp. 967-977, 1998.

[12] Kim, K.y. and Ye, L., Interlaminar fracture toughness of CF/PEI composites at elevated temperature: roles of matrix toughness and fibre/matrix adhesion, Composites Part A: App. Sci. Manufact., 35(4), pp. 477-487, 2004.

[13] ASTM D6671 / D6671M. Standard Test Method for Mixed Mode I-Mode II Interlaminar Fracture Toughness of Unidirectional Fiber Reinforced Polymer Matrix Composites, ASTM Standards Vol. 15, Chap. 3, 2006.

[14] Kenane, M., and Benzeggagh, M.L., Mixed-mode delamination fracture toughness of unidirectional glass/epoxy composites under fatigue loading, Comp. Sci. Tech., 57, pp. 597-605, 1997.

[15] Lander, J.K, Kawashita, L.F., Allegri, G., Hallet, S.R. and Wisnom, M.R., A cut-ply specimen for the determination of mixed-mode interlaminar fracture toughness**.** Proceedings of ECCM 14, Budapest, Hungary, 2010.

[16] Suo., Z., Delamination Specimens for Orthotropic Materials, ASME J. App. Mech., 57, pp. 627-634, 1990.

[17] O'Brien, T.K., Johnston, W.M., Toland, G.J., Mode II Interlaminar Fracture Toughness and Fatigue Characterization of a Graphite Epoxy Composite Material, NASA/TM-2010-216838.